ACS Catalysis
Research Article
pubs.acs.org/acscatalysis

Mechanistic Insights into the Zeolite-Catalyzed Isomerization and Disproportionation of *m*-Xylene

Hyung-Ki Min, Seung Hyeok Cha, and Suk Bong Hong*

Department of Chemical Engineering and School of Environmental Science and Engineering, POSTECH, Pohang 790-784, Korea

Supporting Information

ABSTRACT: The mechanisms of *m*-xylene isomerization and disproportionation over 13 medium-pore zeolites and three large-pore ones are investigated. While H-TNU-10 and H-ZSM-57 with intersecting 10- and 8-ring channels were found to show considerably higher *p*/*o* ratios than H-ZSM-5, a commercial *m*-xylene isomerization catalyst, the GC-MS results from used zeolite catalysts demonstrate the intrazeolitic build-up of tri- and tetramethylated diphenylmethane species, whose existence during the *m*-xylene transformation over any acidic catalyst has not been experimentally verified until now. These dicyclic aromatic compounds were ascertained to serve as reaction intermediates of bimolecular *m*-xylene isomerization within the micropores not only of large-pore zeolites but also of medium-pore materials at temperatures lower than 523 K or so, once there are internal void spaces larger than 10-rings. Flushing experiments with used zeolites followed by GC-MS analyses strongly suggest that the high *p*-xylene selectivity found in some medium-pore zeolites is largely due to product shape selectivity rather than to transition state one. More importantly, the overall GC-MS results of our work demonstrate that transition state and product shape selectivities are experimentally distinguishable from each other.

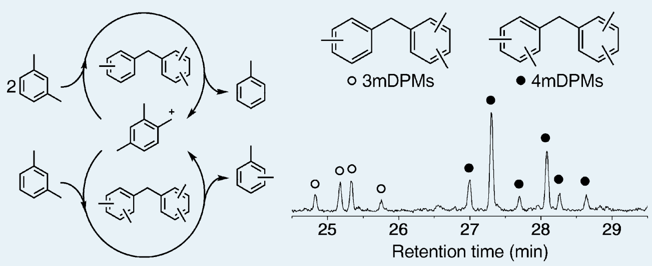

KEYWORDS: *zeolites, m-xylene isomerization, shape selective catalysis, transition states, GC-MS, reaction mechanism*

1. INTRODUCTION

During the last several decades, the high demand of *p*-xylene mainly for the production of terephthalic acid has brought about great progress in *m*-xylene isomerization, toluene alkylation and disproportionation, and ethylbenzene isomerization technologies using aluminosilicate zeolites as shape selective catalysts.[1−4] Among these aromatic processing technologies, *m*-xylene isomerization allows low-valued *m*-xylene to be transformed into a *para*-isomer rich mixture. At present, many commercial isomerization plants based on mordenite (framework type MOR), ZSM-5 (MFI), or EU-1 (EUO) catalyst systems are in operation all over the world.[2,3]

It has long been recognized that the prevailing mechanism of zeolite-catalyzed *m*-xylene isomerization is governed by the pore width of the zeolite employed.[5−12] On large-pore zeolites like H−Y (FAU), *m*-xylene can undergo isomerization to *o*- and *p*-xylenes via a bimolecular mechanism which requires disproportionation and transalkylation involving tri- and tetramethylated diphenylmethane (3mDPM and 4mDPM) derivatives as reaction intermediates, respectively. To our knowledge, however, the existence of these bicyclic aromatic transition states during *m*-xylene transformation over any acidic catalyst has not been experimentally verified until now. Because of the spatial constraints imposed by 10-ring portals, on the other hand, the intramolecular 1,2-methyl shift has been simply in favor with medium-pore zeolites, regardless of the type of their "internal" pore structure. Consequently, *m*-xylene isomerization has been widely used as a probe reaction for distinguishing between medium- and large-pore materials,[13−18] although theoretical work claims that a methoxide-mediated disproportionation pathway of *m*-xylene, involving the less space-demanding exchange of a methyl cation between the zeolite and *m*-xylene, is also possible.[19]

There is a non-negligible number of medium-pore zeolite structures which contain internal cavities/channels larger than 10-rings, e.g., EU-1, MCM-22 (MWW), NU-87 (NES), etc.[20] Thus, the volumes of such void spaces are large enough to accommodate at least some, if not all, of possible reaction intermediates (i.e., a total of 18 3mDPM and 21 4mDPM isomers with different molecular dimensions; see Supporting Information Figure S1) of *m*-xylene disproportionation followed by transalkylation, without experiencing severe geometric constraints. This implies that the actual mechanism of *m*-xylene conversion over medium-pore zeolites could be more complex than what has been believed thus far,[13−18] like the case of ethylbenzene disproportionation, a standard reaction for characterizing acidic zeolite catalysts recommended by the IZA Catalysis Commission.[21−28] Although the high *para*-/*ortho*-isomer (*p*/*o*) and isomerization/disproportionation (*i*/*d*) ratios observed for medium-pore zeolites have often been rationalized by product and transition state shape selectivities, respectively; in particular, no clear experimental evidence which

Received: February 20, 2012
Revised: March 31, 2012
Published: April 18, 2012

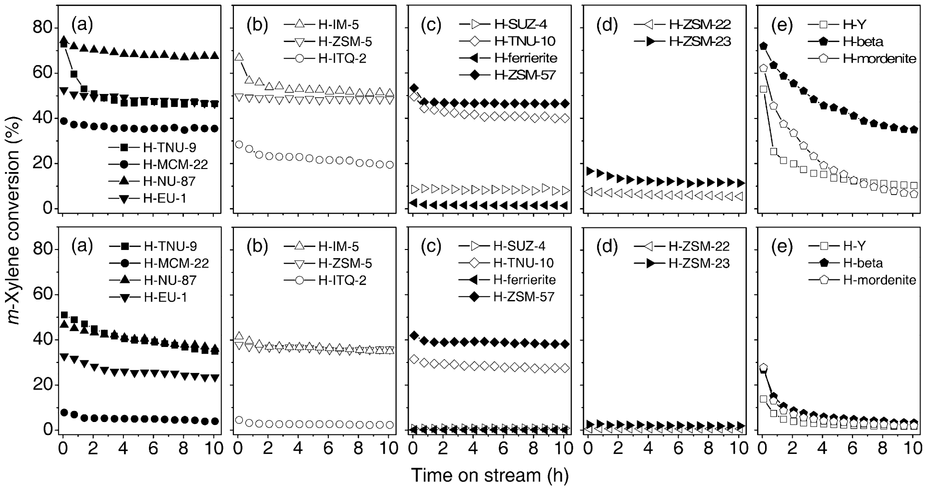

Figure 1. *m*-Xylene isomerization and disproportionation at 10.7 h^{-1} WHSV over medium- and large-pore zeolites with different framework topologies measured at 523 (bottom) and 623 (top) K. The materials studied here include medium-pore zeolites containing (a) large 12-ring cavities, (b) mutually intersecting 10-ring channels only, (c) intersecting 10- and 8-ring channels, (d) 1D 10-ring channels only, and (e) large-pore zeolites.

allows a solid discrimination between these two phenomena has been reported yet.

In this contribution we compare the catalytic properties of 13 medium-pore zeolites with different framework topologies and three well-known large-pore zeolites for the isomerization and disproportionation of *m*-xylene and the ex situ gas chromatography−mass spectrometry (GC-MS) results from all used zeolite catalysts in order to gain new insights into the issues raised above. There is little doubt that direct observation of reaction intermediates on a working catalyst are essential for safely elucidating the type of the shape selective phenomena derived from the particular pore architecture of zeolites. We also carry out isotope labeling experiments during the *p*-xylene transformation in an attempt to estimate the contribution of bimolecular pathway in xylene isomerization over each of zeolites employed here.[7]

2. EXPERIMENTAL SECTION

Catalyst Preparation. NH_4-ZSM-5 (Si/Al = 14), K-ferrierite (Si/Al = 9), and Na-mordenite (Si/Al = 10) were obtained from Tosoh, and H−Y (Si/Al = 15) and NH_4-beta (Si/Al = 13) were purchased from PQ. To ensure that these zeolites were completely in their proton form, they were refluxed twice in 1.0 M NH_4NO_3 solutions (2.0 g solid per 100 mL solution) for 6 h followed by calcination at 823 K for 4 h. All other zeolites were prepared according to the procedures described in the literature.[28−39] As-made zeolites were calcined in air at 823 K for 8 h to remove the organic structure-directing agents occluded. The calcined materials were then converted into their proton form following the procedures similar to those given above. Prior to use as catalysts, acidic zeolites were granulated by pressing without a binder under a maximum pressure of 2.8×10^7 Pa, crushed, and sieved to obtain particles with a diameter of 0.2−0.3 mm.

Analytical Methods. The crystallinity and phase purity of zeolites prepared in this work were determined by powder X-ray diffraction (XRD) on a PANalytical X'Pert diffractometer (Cu Kα radiation). Their powder XRD patterns show that each of them is highly crystalline and no impurity phases are detected (Supporting Information Figure S2). Elemental analysis was carried out on a Jarrell-Ash Polyscan 61E inductively coupled plasma spectrometer in combination with a Perkin-Elmer 5000 atomic absorption spectrophotometer. N_2 sorption experiments were made with a Mirae SI nanoPorosity-XQ analyzer. Crystal morphology and size were determined by a JEOL JSM-6510 scanning electron microscope (SEM). The acidic properties of all zeolites employed here were characterized by infrared (IR) spectroscopy using pyridine as a probe molecule. Pyridine adsorption−desorption measurements were carried out on self-supporting zeolite wafers of ca. 9 mg cm^{-2} activated under vacuum at 773 K for 2 h. After contacting with pyridine vapor (6.0×10^2 Pa) at 373 K for 0.5 h inside a home-built IR cell with CaF_2 windows followed by desorption (10^{-1} Pa) at 573 K for 2 h, the IR spectra were recorded on an ABB Bomem MB 104 FT-IR spectrometer. The concentrations of Brønsted and Lewis acid sites were determined from the intensities of the IR bands around 1550 and 1450 cm^{-1}, respectively, by using the extinction coefficients given by Emeis.[40]

The organic compounds formed on the zeolite catalysts after *m*-xylene reactions at different temperatures and periods of time-on-stream (TOS) were extracted by a modification of the procedure originally developed by Guisnet and co-workers.[41] In a typical GC-MS analysis, 50 mg of the used catalyst were completely dissolved in 3 mL of 10% HF solutions and neutralized with K_2CO_3. The organic species from the resulting solution were extracted by CH_2Cl_2 (Aldrich, 99.9%), and residual water in the organic phase was removed by adding a small amount of Na_2SO_4 that was subsequently recovered using an Advantec DISMIC-13JP syringe filter. The GC-MS total ion chromatograms were recorded on a Varian CP 3800 gas chromatograph equipped with a Varian 320-MSD mass selective detector. Further details of GC-MS analysis can be found in our recent studies.[42,43] The organic compounds extracted were identified by comparing with the NIST database.[44]

Catalysis. The isomerization and disproportionation of *m*-xylene were conducted under atmospheric pressure in a continuous-flow microreactor. Each catalyst was activated under flowing N_2 (50 mL min^{-1}) at 773 K for 2 h and kept at the desired reaction temperature, allowing time for the reactant/carrier gas distribution to be stabilized. Then, *m*-

Table 1. Crystallographic Dimensions of 10-Ring Pores and Channel Intersections or Cavities in Zeolites with Different Pore Topologies Employed in This Study

zeolite	IZA code	pore topology	10-ring pore size (Å)[a]	channel intersection or cavity dimension (Å)[b]
H-TNU-9	TUN	3D, 10-rings + 12-ring cavities	5.5 × 5.6 (24.2, 0.19), 5.4 × 5.5 (23.3, 0.19)	5.3 × 10.9 × 15.7
H-MCM-22	MWW	2D, 10-rings + large cages	4.0 × 5.5 (17.3, 0.69), 4.1 × 5.1 (16.4, 0.59)	7.0 × 7.0 × 18.7 (7.1 × 7.1 × 18.2)
H-NU-87	NES	2D, 10- and 12-rings	4.8 × 5.7 (21.5, 0.54), 5.3 × 7.8[c]	5.3 × 7.8 × 19.0
H-EU-1	EUO	1D, 10-rings + side pockets	4.1 × 5.4 (17.4, 0.65)	5.1 × 6.8 × 14.0
H-IM-5	IMF	3D, 10-rings	5.5 × 5.6 (24.2, 0.19), 5.3 × 5.4 (22.5, 0.19), 5.3 × 5.9 (24.6, 0.44), 4.8 × 5.4 (20.4, 0.46), 5.1 × 5.3 (21.2, 0.27)	10.4
H-ZSM-5	MFI	3D, 10-rings	5.1 × 5.5 (22.0, 0.37), 5.3 × 5.6 (23.3, 0.32)	8.6
H-ITQ-2		2D, 10-rings	4.1 × 5.1 (16.4, 0.59)	7.2
H-SUZ-4	SZR	3D, 10 and 8-rings	4.1 × 5.2 (16.7, 0.61)	9.8
H-TNU-10	STI	2D, 10 and 8-rings	4.7 × 5.0 (18.5, 0.34)	8.4
H-ferrierite	FER	2D, 10 and 8-rings	4.2 × 5.4 (17.8, 0.63)	8.3
H-ZSM-57	MFS	2D, 10 and 8-rings	5.1 × 5.4 (21.6, 0.33)	11.7
H-ZSM-22	TON	1D, 10-rings	4.6 × 5.7 (20.6, 0.59)	
H-ZSM-23	MTT	1D, 10-rings	4.5 × 5.2 (18.4, 0.50)	
H−Y	FAU	3D, 12-rings	7.4 × 7.4[c]	12.0 × 12.0 × 12.0
H-beta	*BEA	3D, 12-rings	6.6 × 6.7[c], 5.6 × 5.6[c]	13.9
H-mordenite	MOR	2D, 12 and 8-rings	6.5 × 7.0[c]	

[a] The values in parentheses are the area in squared angstroms and ellipticity of 10-ring pores. The pore area was calculated using the equation $A = \pi ab/4$, where A, a, and b are the pore area and the shortest and longest pore diameters, respectively. The pores in each zeolite are assumed to be ideally elliptical in shape. Ellipticity can be defined as $\{(b^2 - a^2)/b^2\}^{0.5}$.[47] [b] Dimensions of channel intersections or cavities calculated using the CrystalMaker Software. The values in parentheses are those reported in the literature.[20] [c] 12-ring pore size.

xylene (99%, Aldrich) with a partial pressure of 2.0×10^4 Pa in N_2, which was purified by passing through a column filled with alumina to remove oxygenated aromatic impurities, was fed into the microreactor containing 0.2 g of zeolite catalyst at a weight hourly space velocity (WHSV) of 10.7 h^{-1}. The reaction products were analyzed online in a Varian CP-3800 gas chromatograph equipped with a CP-Chirasil-Dex CB capillary column (25 m × 0.25 mm) and a flame ionization detector, with the first analysis carried out after 5 min on stream. Since all zeolites studied here showed catalyst deactivation, their initial reaction rates and product distributions were obtained by extrapolating the time dependent data to zero TOS. Mass balances were within ±3% of closure in all cases. Isotope labeling experiments using an equimolar mixture of 1.0×10^4 Pa normal *p*-xylene ($C_6H_4(CH_3)_2$, 99%, Aldrich) and 1.0×10^4 Pa hexadeuterated *p*-xylene ($C_6H_4(CD_3)_2$, 98 atom % D, Cambridge Isotope Laboratories) in N_2 were also performed at 523 K in the same reactor. The products were collected between 0 and 60 s and then analyzed by GC-MS. To keep the conversion lower than 10%, WHSV was adjusted by varying the weight of catalyst between 0.01 and 0.2 g.

Flushing experiments, in which the *m*-xylene-containing stream was replaced by pure N_2 stream (40 mL min^{-1}), were carried out as a function of time at a given temperature. Prior to these experiments, the catalyst was reacted with *m*-xylene at 473 K for 10 h, cooled quickly to room temperature, and divided into a series of batches with exactly the same amount (50 mg). Then, each batch was flushed in a pure N_2 stream at a given temperature for different periods of time. The flushed catalyst was subjected to exactly the same HF dissolution procedures as those described elsewhere,[42,43] to follow the evolution of the organic compounds accumulated within the zeolite micropores with increasing flushing time.

3. RESULTS AND DISCUSSION

Figure 1 shows *m*-xylene conversion as a function of TOS at 10.7 h^{-1} WHSV in *m*-xylene isomerization and disproportionation over 13 medium-pore zeolites with different framework structures, as well as over 3 common large-pore zeolites, measured at 523 and 623 K, respectively. The structural features of zeolite catalysts employed in this work are compared in Table 1,[20] and their textural and acidic properties determined by N_2 sorption and IR spectroscopy with adsorbed pyridine, respectively, can be found in Supporting Information Table S1. Given that variations in Al content and crystallite size of all 16 zeolites are not so wide, the catalytic data in Figure 1 could illustrate the shape selectivity effects imposed by the unique pore structure of each zeolite.

When *m*-xylene transformation is carried out at 523 K, H-TNU-9 (TUN) and H-NU-87 show a higher *m*-xylene conversion than H-ZSM-5, a commercial catalyst for this reaction, at early TOS. While these medium-pore zeolites give a gradual decrease in conversion with increasing TOS, their conversions are notably higher than the conversion over any of large-pore materials H−Y, H-beta (*BEA), and H-mordenite in which the isomerization and disproportionation of *m*-xylene can proceed via the bimolecular mechanism catalyzed by Brønsted acid sites.[5−12] The lowest conversion among the medium-pore zeolites containing 12-ring cavities was observed for H-MCM-22 with large cylindrical cages (7.1 Å in diameter and 18.2 Å in height). The shortest dimensions (4.0 or 4.1 Å) of 10-ring portals in H-MCM-22 are fairly smaller than those (5.4 or 5.5 and 4.8 Å) of the analogous portals in H-TNU-9 and H-NU-87 (Table 1). Thus, the intracrystalline diffusivity of *m*-xylene molecules with a kinetic diameter of 6.8 Å[45] should be smaller in H-MCM-22, which imparts a considerably low *m*-xylene conversion to this medium-pore zeolite. It is worth noting that H-ITQ-2, the delaminated analog of H-MCM-22, shows a marginally lower conversion than H-MCM-22 during the period of TOS studied here. Since H-ITQ-2 has an external

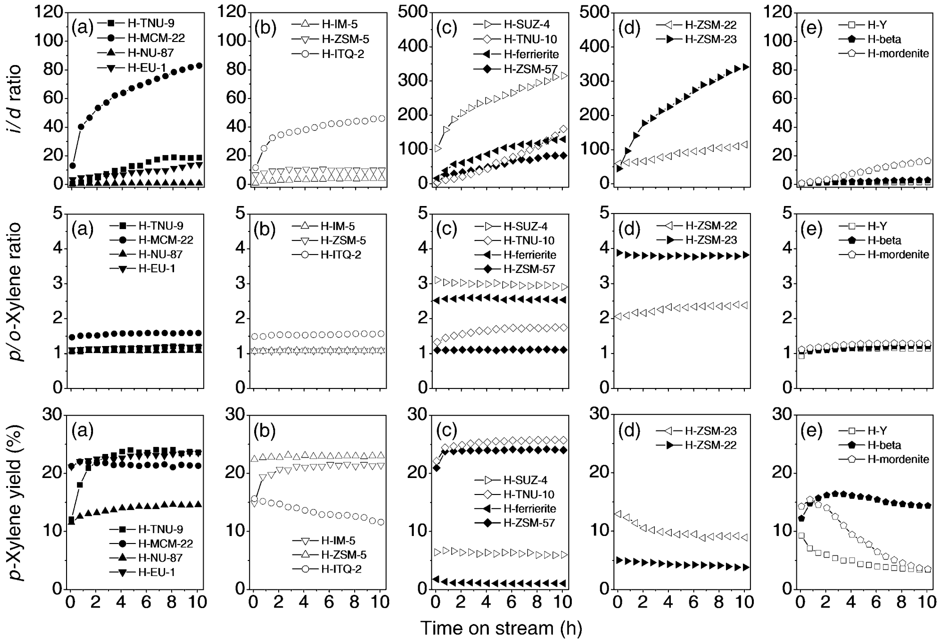

Figure 2. *p*-Xylene yield (bottom) and *p*/*o* (middle) and *i*/*d* (top) ratios as a function of time on stream in *m*-xylene transformation over medium- and large-pore zeolites with different framework topologies at 623 K and 10.7 h^{-1} WHSV. The zeolite catalysts employed are medium-pore zeolites containing (a) 12-ring cavities, (b) mutually intersecting 10-ring channels only, (c) intersecting 10- and 8-ring channels, (d) 1D 10-ring channels only, and (e) large-pore zeolites.

surface area about seven times larger than that of its parent zeolite (Supporting Information Table S1), the contribution of acid sites in structurally well-defined external 12-ring pockets to its overall catalytic action appears to be considerably lower than that of acid sites in two-dimensional (2D) sinusoidal 10-ring channels. This speculation is also applicable to the acid sites in 12-ring side pockets located on the external surface of EU-1 crystallites.[20,46]

As seen in Figure 1, on the other hand, H-IM-5 (IMF) is characterized by an essentially identical *m*-xylene conversion with that of H-ZSM-5 at both 523 and 623 K. This can be explained by considering its pore system consisting of mutually intersecting 10-ring channels only. Of particular interest is the observation that H-TNU-10 (STI) and H-ZSM-57 (MFS) show slightly lower and higher conversions at 523 K than H-ZSM-5, respectively, which remain nearly constant during 10 h on stream, whereas H-SUZ-4 (SZR) and H-ferrierite (FER) exhibit almost zero conversion. A similar trend was also found at 623 K. As seen in Figure 2, more importantly, the *p*-xylene yield of H-TNU-10 is higher than that of H-ZSM-5, H-IM-5, or H-ZSM-57 during 10 h on stream at this reaction temperature. While the *m*-xylene conversions at 623 K of these four medium-pore zeolites after ca. 2 h on stream are in the rather narrow range (48 ± 4%), H-TNU-10 gives a *p*/*o* ratio higher than any of the other three zeolites during the rest of the period of TOS studied. This suggests its capability of being a more efficient isomerization catalyst than H-ZSM-5, which can be further supported by the continuous increase in *i*/*d* ratio during the period of TOS studied here (Figure 2). After 10 h on stream, in consequence, the *i*/*d* ratio of H-TNU-10 becomes much higher than the value of any of H-ZSM-5, H-IM-5, and H-ZSM-57.

The structural data in Table 1 indicate that while all of TNU-10, ZSM-57, ferrierite, and SUZ-4 possess intersecting 10- and 8-ring channels, the area (18.5 Å^2) of 10-ring channels in TNU-10 is slightly smaller and larger than the areas (21.6 and 17.8 or 16.7 Å^2) of the analogous channels in ZSM-57 and in ferrierite or SUZ-4, respectively. Since the shape of zeolite pores, as well as their size, is a critical factor affecting the intrazeolitic diffusional features of both reactant and product molecules,[1] we have focused our attention on the ellipticity defined by $\{(b^2 - a^2)/b^2\}^{0.5}$,[47] where a and b are the shortest and longest pore diameters, respectively, as a quantitative measure of differences in the 10-ring pore shape of zeolites studied here. As listed in Table 1, the ellipticity (0.61 or 0.63) of 10-ring channels in SUZ-4 or ferrierite is considerably larger than the value (0.34) of the analogous channels in TNU-10. If such is the case, the more elliptical 10-ring channels in the former two zeolites would then have more severe steric constraints in the diffusion of *m*-xylene. However, the actual situation is not so simple, because H-EU-1, H-MCM-22, and H-ITQ-2, the 10-ring pore areas (16.4−17.4 Å^2) and ellipticities (0.59−0.69) of which are essentially identical with those (17.8 Å^2 and 0.63) in H-ferrierite, show considerably higher conversions than the latter zeolite at 623 K. We also note that H-ZSM-22 (TON) exhibits a much poorer activity than H-NU-87 at both 523 and 623 K, although their 10-ring pore dimensions (4.6 Å × 5.7 Å and 4.8 Å × 5.7 Å) are quite similar to each other. These results cannot be rationalized without suggesting that the topological flexibility of zeolites[48−51] is another important factor influencing the intracrystalline diffusivity of *m*-xylene. Since zeolite framework topology is generally considered as built from quite stiff TO_4 tetrahedra joined through rather floppy O linkages, where T is Si or Al, the built-in flexibility of T−O−T angle connector between TO_4 units can allow each of zeolite structures to contract and expand at a different level upon response to thermodynamic variables like temperature, as well as upon variations in framework composition.

Figure 3 shows plots of the concentration of Brønsted acid sites (Supporting Information Table S1) in a series of medium-pore zeolites with different framework topologies determined from IR spectroscopy with adsorbed pyridine, the pore dimensionality of each zeolite structure, and its largest portal

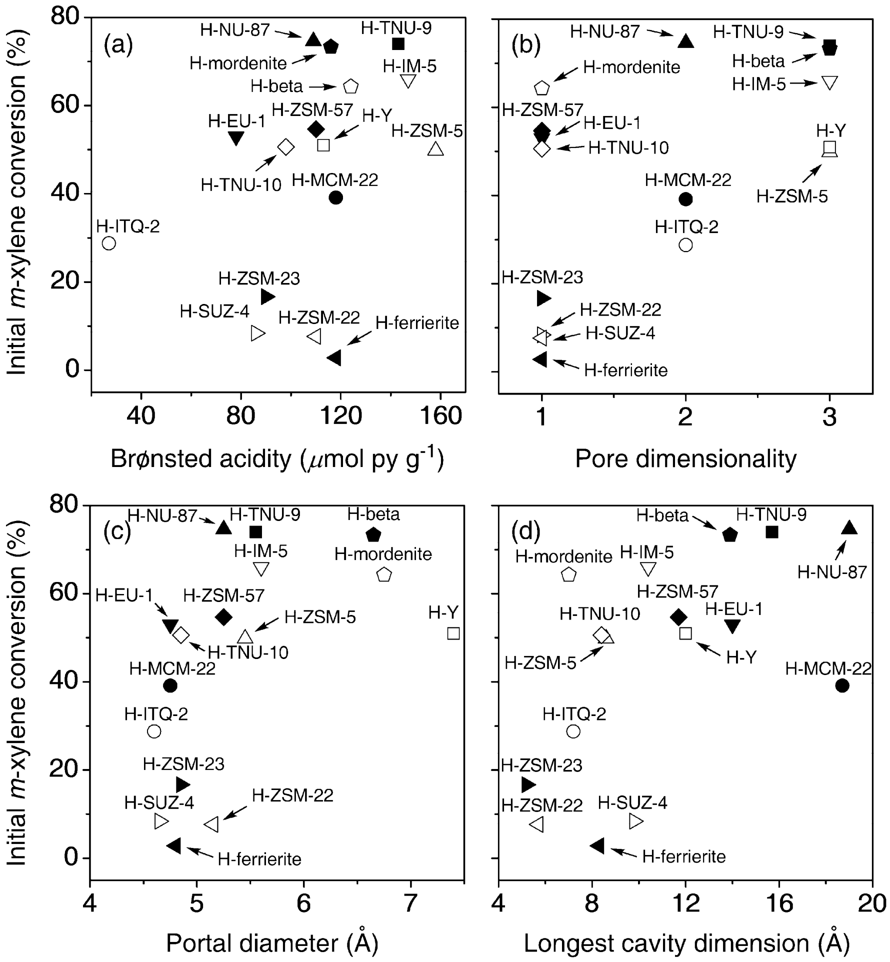

Figure 3. Plots of initial *m*-xylene conversion at 623 K and 10.7 h^{-1} WHSV versus (a) concentration of Brønsted acid sites in a total of 16 acidic zeolites with different framework structures determined from IR spectroscopy with adsorbed pyridine, (b) pore dimensionality of each zeolite topology, and its (c) portal diameter and (d) longest cavity dimension or channel intersection diameter.

Table 2. *p*/*o*, *i*/*d*, and 1,2,3-TMB/1,3,5-TMB Ratios and TMB Distribution at 623 K and Initial *m*-Xylene Conversions near 20% over Medium- and Large-Pore Zeolites with Different Framework Topologies

				normalized TMB distribution (mol %)			
zeolite	initial conversion (%)[a]	*p*/*o* ratio	*i*/*d* ratio	1,2,3-TMB	1,2,4-TMB	1,3,5-TMB	1,2,3-TMB/1,3,5-TMB ratio[b]
H-TNU-9	21.3	3.2	5	0.7	99.1	0.2	
H-MCM-22	18.2	2.0	12	7.6	76.2	16.2	0.47
H-NU-87	22.6	1.7	8	1.9	97.6	0.5	
H-EU-1	22.2	2.3	60	1.6	96.8	1.6	
H-IM-5	22.1	3.2	34	4.1	92.7	3.2	
H-ZSM-5	21.9	2.5	114	0.0	100	0.0	
H-ITQ-2	19.2	1.4	21	8.6	69.2	22.2	0.39
H-SUZ-4	19.1	2.6	35	6.0	69.5	24.5	0.24
H-TNU-10	20.0	4.4	21	0.0	100	0.0	
H-ZSM-57	22.4	4.9	213	5.3	89.4	5.3	1.00
H-ZSM-23	19.2	3.4	27	4.5	77.8	17.7	0.25
H−Y	17.4	1.1	1	7.7	64.1	28.2	0.27
H-beta	19.2	1.2	2	8.3	64.9	26.8	0.31
H-mordenite	22.1	1.3	3	8.8	72.5	18.7	0.47
equilibrium[c]		1.1		8.0	68.0	24.0	0.33

[a] Initial *m*-xylene conversion was adjusted to ca. 20% by varying WHSV from 0.04 to 24 h^{-1}. [b] When 1,2,4-TMB selectivity was greater than 90%, the 1,2,3-TMB/1,3,5-TMB ratio was not given because of the possible inaccuracy in selectivity to 1,2,3-TMB and/or 1,3,5-TMB. [c] From ref 13.

diameter (average diameter, when the portals are noncircular) and longest cavity dimension or channel intersection diameter vs the initial *m*-xylene conversion at 623 K and 10.7 h^{-1} WHSV. The initial conversions of large-pore materials H−Y, H-beta, and H-mordenite are also compared in Figure 3. Here, H-mordenite and all medium-pore zeolites with intersecting 10-

and 8-ring channels were considered as 1D materials, since the diffusion of *m*-xylene molecules is not feasible within their small 8-rings. A lack of correlation between the zeolite acidity and the initial *m*-xylene conversion was found. Although H-TNU-9 has a lower concentration of Brønsted acid sites than H-ZSM-5, for example, the former zeolite exhibits a considerably higher conversion than the latter one. A similar trend can also be observed when the initial conversion is plotted against any of the three structural factors stated above. Therefore, it appears that the *m*-xylene reactivity of medium-pore zeolites can be simply understood in terms of neither their acidity nor particular structural parameter.

Table 2 lists the *p*/*o*, *i*/*d*, and 1,2,3-trimethylbenzene (TMB)/1,3,5-TMB ratios and the TMB distribution at 623 K and initial *m*-xylene conversion levels near 20% over a wide variety of medium-pore zeolites with different framework structures, as well as over three well-known large-pore materials. The catalytic data for H-ferrierite and H-ZSM-22 were not included, because it was not possible to gain conversions higher than 10% over them under the reaction conditions described above. The *p*/*o* ratios of well-known zeolites in Table 2 were found to be in reasonable agreement with the values reported in the literature.[15,52] For example, H-ZSM-5 and H−Y show *p*/*o* ratios of 2.5 and 1.1, typical of medium-pore and large-pore zeolites, respectively.[13−15] As commented earlier, in addition, H-TNU-10 and H-ZSM-57 exhibit the two highest *p*/*o* ratios among the zeolites studied here, confirming their potential to be efficient *m*-xylene isomerization catalysts. On the other hand, the higher *p*/*o* ratio (3.4) observed for the 1D medium-pore zeolite H-ZSM-23 can be attributed to its low concentration of acid sites (Supporting Information Table S1), as well as to the smaller 10-ring (4.5 × 5.2 Å) channels. Then, the extent of the nonshape selective secondary isomerization of xylenes on the external surface of H-ZSM-23 may be low compared with that of the other medium-pore zeolites, giving a relatively higher *p*/*o* ratio. As repeatedly reported,[15,52] however, the *p*/*o* ratio (1.7) of H-NU-87 is in the expected range for large-pore materials.

According to the previous work on the reactions of 1,2,4-TMB over this medium-pore zeolite at 623 K,[53] isomerization to 1,2,3- and 1,3,5-isomers occurs largely on its external surface, which has been ascertained by the selective poisoning experiments of external acid sites, unlike the disproportionation that proceeds mainly within the H-NU-87 pores. In fact, if a portion of the external surface of H-NU-87 crystallites is terminated by 12-ring pockets that form as a result of the truncation of 12-ring cavities with four 10-ring windows along the *a* axis,[20] the contribution of the external acid sites to its overall catalytic action during the *m*-xylene isomerization and disproportionation cannot be underestimated. Then, the *p*/*o* ratio of this medium-pore zeolite can be reasoned to be relatively low as listed in Table 2. A similar interpretation can be given to the low *p*/*o* ratio (1.4) of H-ITQ-2 with an extremely high external surface area. Table 2 also shows that the *i*/*d* ratios (5−12) of H-TNU-9, H-MCM-22, and H-NU-87 are considerably lower than the ratios of typical medium-pore zeolites like H-ZSM-5,[15,17] which can be correlated with their large 12-ring cavities. *m*-Xylene disproportionation is bimolecular in nature so that its reaction pathway is much more space-demanding than the monomolecular *m*-xylene isomerization mechanism (i.e., an intramolecular 1,2-methyl shift).[5−12]

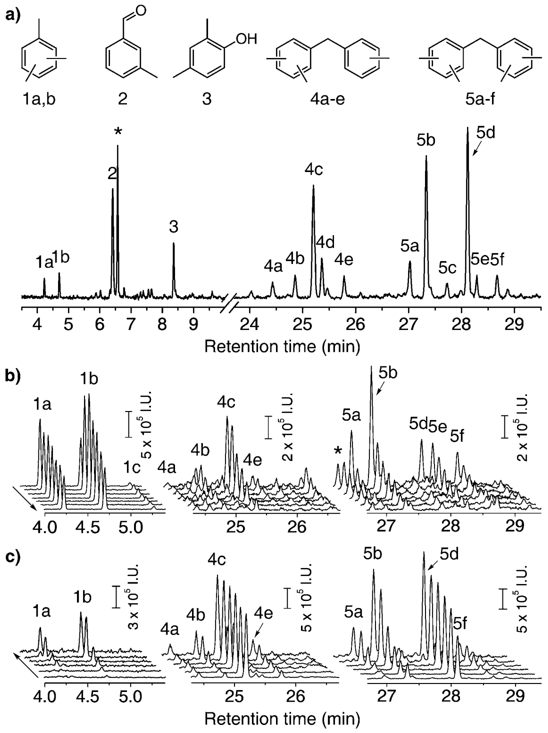

Figure 4. (a) GC-MS total ion chromatogram of the CH_2Cl_2 extract from H-TNU-9 after *m*-xylene isomerization and disproportionation at 403 K for 10 h on stream. The structures annotated above the chromatogram are peak identifications made by comparing the mass spectra with those in the NIST database,[44] and the peak indicated by an asterisk is the mass signal of C_2Cl_6 used as an internal standard. (b) GC-MS chromatograms of the CH_2Cl_2 extract from H-TNU-9 after *m*-xylene transformation at 473 K for 10 h on stream followed by flushing with N_2 (40 mL min^{-1}) at the same temperature for 0, 2, 5, 10, 30, 60, and 120 min, respectively. The peak indicated by an asterisk is the mass signal of methylphenanthrenes formed within the H-TNU-10 micropores. (c) GC-MS chromatograms of the CH_2Cl_2 extract from H-TNU-9 after *m*-xylene transformation at 403 K for 5, 30, 60, 120, 300, and 600 min on stream, respectively.

Figure 4 shows the GC-MS total ion chromatogram of the CH_2Cl_2 extract from H-TNU-9 containing 12-ring cavities limited by its main and short bridging 10-ring channels after *m*-xylene isomerization and disproportionation at 403 K and 10.7 h^{-1} WHSV for 10 h on stream, where conversions of ca. 1% at the steady state were achieved. While hydrocarbons $\leq C_8$ cannot be analyzed owing to the inevitable mass detector saturation by the CH_2Cl_2 solvent, weak peaks 1a and 1b have mass spectra and retention times corresponding to 1,3,5- and 1,2,4-TMB isomers, respectively. In contrast, stronger peaks 2 and 3 represent 3-methylbenzaldehyde and 2,4-dimethylphenol, respectively. Because no significant amounts of oxygenated aromatic impurities are present in the feed, these compounds appear to be formed from chemisorbed *m*-xylene molecules on the Brønsted acid sites in H-TNU-9 during the HF dissolution. On the other hand, the compounds responsible for peaks 4a−e have a molecular mass of 210, equivalent to a $C_{16}H_{18}$ hydrocarbon. When compared to the NIST database,[44] their ion mass distributions (Supporting Information Figure S3) were found to be the same as those of five out of the 18 possible 3mDPM isomers, transition states of *m*-xylene disproportionation to benzene and TMBs. But the exact positions of their methyl groups remain uncertain due to the lack of the authentic compounds. The other important compounds in Figure 4a are those represented by peaks 5a−

f: all of them have a molecular mass of 224 and thus a molecular formula of $C_{17}H_{20}$. The NIST database reveals that the ion mass distributions (Supporting Information Figure S4) for these six peaks correspond to 4mDPM species, transition states of transalkylation between *m*-xylene and TMBs, although their unequivocal assignment among the 21 possible 4mDPM isomers (Supporting Information Figure S1) cannot be made at this time for the same reason stated above.

To clarify the role of 3mDPM and 4mDPM species as reaction intermediates of *m*-xylene isomerization and disproportionation, we reacted H-TNU-9 with *m*-xylene at 473 K for 10 h on stream, where the catalyst showed conversions of around 15% at the pseudosteady state. Then, we divided the resulting catalyst into a series of batches with exactly the same amount (50 mg) and flushed them in a pure N_2 stream (40 mL min^{-1}) at the same temperature for times up to 120 min. As seen in Figure 4b, peak 1a due to 1,3,5-TMB formed within the H-TNU-9 pores gives a continuous decrease in intensity with increasing flushing time. However, peak 1b corresponding to 1,2,4-TMB increases at the onset of flushing, levels off, and then decreases after 5 min. Since this is in line with the continuous decrease in intensity of the 3mDPM and 4mDPM signals with increasing flushing time, both derivatives may be unstable enough to decompose into xylenes and 1,2,4-TMB at 473 K. It is noteworthy that their GC-MS signals become strongest when reacted with *m*-xylene over H-TNU-9 at 473 K (Supporting Information Figure S5).

We also monitored the generation of 3mDPM and 4mDPM derivatives as a function of TOS in H-TNU-9 during the *m*-xylene transformation at 403 K and 10.7 h^{-1} WHSV by using GC-MS. As seen in Figure 4c, the most prominent peak 4c among the five peaks due to 3mDPM derivatives is almost saturated even after 5 min on stream. However, the other four peaks show a continuous increase in intensity during 5 h on stream. This can be rationalized by suggesting that the 3mDPM isomer responsible for peak 4c may be transformed into its thermodynamically more stable isomers inside the TNU-9 pores. It has long been recognized that the isomerization of three different carbocations with a DPM backbone initially formed as reaction intermediates of *m*-xylene disproportionation to give 1,2,3-, 1,2,4-, and 1,3,5-TMBs, respectively (Supporting Information Scheme S1), is possible not only via a bimolecular transalkylation when sufficiently spacious, but also via a monomolecular methyl-transfer reaction when highly confined.[54−57] Considering that H-TNU-9 shows almost 100% selectivity to 1,2,4-TMB (Table 2), peak 4c can be tentatively assigned to the 2,4-dimethyl-1-(3-methylbenzyl)benzene isomer among the 18 possible 3mDPM isomers. Figure 4c also shows that after some TOS peak 5d gives no significant intensity changes, unlike the other five peaks characterized by a continuous increase in intensity during the period of TOS studied here. We speculate that the 4mDPM isomer represented by peak 5d may be thermodynamically less stable than the other five 4mDPM isomers, undergoing isomerization, as peak 4c behaves. From Figure 4, therefore, it is clear that both 3mDPM and 4mDPM derivatives are real transition states of *m*-xylene isomerization and disproportionation over H-TNU-9, primarily due to the presence of large 12-ring cavities in this medium-pore zeolite.

The GC-MS results presented thus far provide clear experimental evidence supporting the bimolecular mechanism of *m*-xylene isomerization proposed in Scheme 1. For example, the formation of the *m*-tolylmethylium cation (**B**) by hydride abstraction upon adsorption of *m*-xylene molecules (**A**) on the Brønsted acid sites in zeolites,[58,59] which initiates disproportionation, can be corroborated by the appearance of the 3-methylbenzaldehyde signal (peak 2) in Figure 4a. Also, the generation of the (2,4-dimethylphenyl)methylium ion (**F**) by splitting of benzenium-type carbocations (**E**),[58,59] which begins transalkylation, can be evidenced by the emergence of the 1,2,4-TMB signal (peak 1b). In particular, the presence of the 1,3,5-TMB signal (peak 1a) in Figure 4a indicates that isomerization of species **F** to (3,5-dimethylphenyl)methylium or (2,3-dimethylphenyl)methylium ions inside the TNU-9 pores is possible. This can be further supported by the GC-MS chromatograms in Figure 4b which clearly show all three TMB isomer signals. In contrast, the observation of 4mDPM derivatives (**J**), as well as of 3mDPM ones (**D**), implies that the hydride abstraction and transfer (i.e., (2,4-dimethylphenyl)-methylium ion **F** to species **B**) have the highest energy barrier among the elementary reactions in Scheme 1, as theoretically predicted.[11] The same conclusion has been drawn from the disproportionation of toluene[58] and ethylbenzene.[27,28] As seen in Scheme 1, therefore, a thermodynamically favorable route is the transalkylation between species **F** and another *m*-xylene molecule which cannot start without disproportionation. But, once **F** is formed, transalkylation can operate by itself to produce a xylene mixture (**L**).

Scheme 1. Bimolecular Diphenylmethane-Mediated Reaction Pathway of the Zeolite-Catalyzed *m*-Xylene Isomerization Proposed Based on the Overall GC-MS Results of This Work

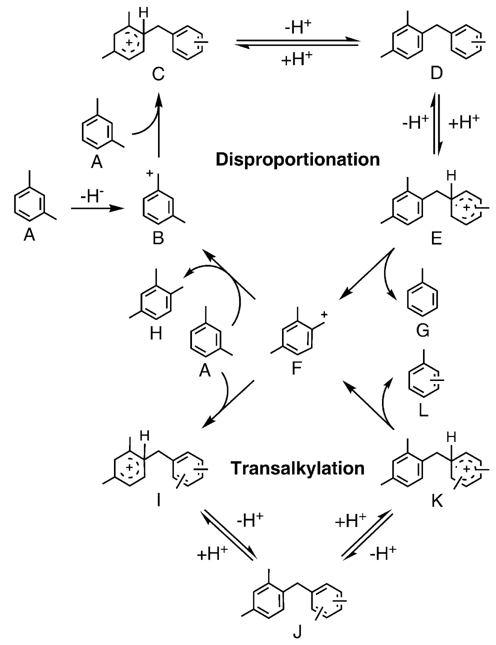

Figure 5 shows the GC-MS chromatograms of the CH_2Cl_2 extracts from a total of 16 medium- or large-pore zeolites with different framework structures after *m*-xylene reactions at 523 K and 10.7 h^{-1} WHSV for 10 h on stream. It can be seen that the formation of both 3mDPM and 4mDPM species is possible not only in medium-pore zeolites containing 12-ring cavities (i.e., H-MCM-22, H-NU-87, and H-EU-1) other than H-TNU-9, but also in those with mutually intersecting 10-ring channels (i.e., H-IM-5 and H-ZSM-5). This is also the case of H-TNU-10 and H-ZSM-57 with a 2D intersecting 10- and 8-ring pore

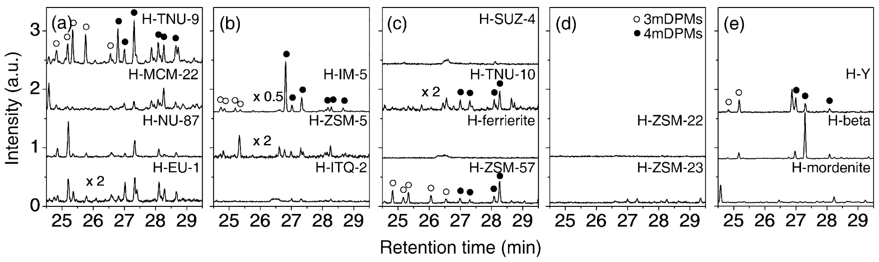

Figure 5. GC-MS total ion chromatograms of the CH_2Cl_2 extracts from 13 medium-pore and three large-pore zeolites with different framework topologies after *m*-xylene isomerization and disproportionation at 523 K and 10.7 h^{-1} WHSV for 10 h on stream. The zeolite catalysts employed include medium-pore zeolites containing (a) large 12-ring cavities, (b) mutually intersecting 10-ring channels only, (c) intersecting 10- and 8-ring channels, (d) 1D 10-ring channels only, and (e) large-pore zeolites. Open and closed circles indicate 3mDPM and 4mDPM species, respectively. For simplicity, only the segments covering the 3mDPM and 4mDPM peaks are shown.

system. However, the GC-MS chromatograms from H-SUZ-4 and H-ferrierite with quite similar architectures show neither 3mDPM signals nor 4mDPM ones. As seen in Figure 5, on the other hand, there are no noticeable signals in the chromatograms from 1D medium-pore zeolites H-ZSM-22 and H-ZSM-23, as well as from H-mordenite, an actually 1D large-pore material with respect to *m*-xylene. This suggests that pore dimensionality is another critical factor affecting the formation of 3mDPM and 4mDPM derivatives during the isomerization and disproportionation over zeolitic catalysts.

The most important observation obtained from Figure 5 is that the number of 3mDPM and 4mDPM signals, as well as their relative intensities, differs notably according to the pore topology of zeolite catalysts. As described above, for example, five 3mDPM signals are observable in the GC-MS chromatogram from H-TNU-9. However, three or four signals can be found in the chromatograms from H-ZSM-5 and H-IM-5. Also, only two signals are detectable from 3D large-pore zeolites H−Y and H-beta. These results indicate that the secondary isomerization of DPM-type intermediates to thermodynamically more stable isomers inside the zeolite pores, as well as their initial formation, is substantially influenced by differences in the local zeolite pore shape and size. Thus, if the internal void spaces of zeolite catalysts employed are large enough to accommodate some DPM-type intermediates during the *m*-xylene transformation, materials with a more confined internal space may tend to stabilize smaller intermediates whose shape and size match well with those of local zeolite pores. This implies that the number of detectable 3mDPM or 4mDPM derivatives should be larger in medium-pore zeolites than in large-pore ones as seen in Figure 5, probably due to the suppression of the secondary isomerization of DPM species imposed by the narrower void spaces of the former materials.

Figure 6 shows the GC-MS chromatograms of the CH_2Cl_2 extracts from H−Y, H-ZSM-5, H-ZSM-57, and H-TNU-10 after *m*-xylene isomerization and disproportionation at 473 K and 10.7 h^{-1} WHSV for 10 h on stream followed by flushing with N_2 at the same temperature for different times. All 3mDPM and 4mDPM species generated in H−Y were found to be completely missing within 2 min of flushing. Given the large H−Y supercages with a diameter of 12.0 Å, this is not surprising.[13−18] We also note that a larger amount of methylphenanthrenes known as coke precursors[60,61] is formed in H−Y then in medium-pore zeolites upon reaction with *m*-xylene at 473 K for 10 h on stream. Compared with those from H-TNU-9 (Figure 4), on the other hand, the GC-MS chromatograms from H-ZSM-5 exhibit no significant differences in the rate of intensity decrease of 3mDPM and 4mDPM signals with increasing flushing time. Unlike the case of H-TNU-9 characterized by a continuous decrease in intensity of the 1,3,5-TMB signal, however, both 1,3,5- and 1,2,4-TMB signals from the latter zeolite increase at the beginning of flushing, level off, and then decrease after 10 min. It thus appears that the intrazeolitic decomposition pattern of DPM-based intermediates, as well as their formation one, is influenced by the pore architecture of zeolite hosts.

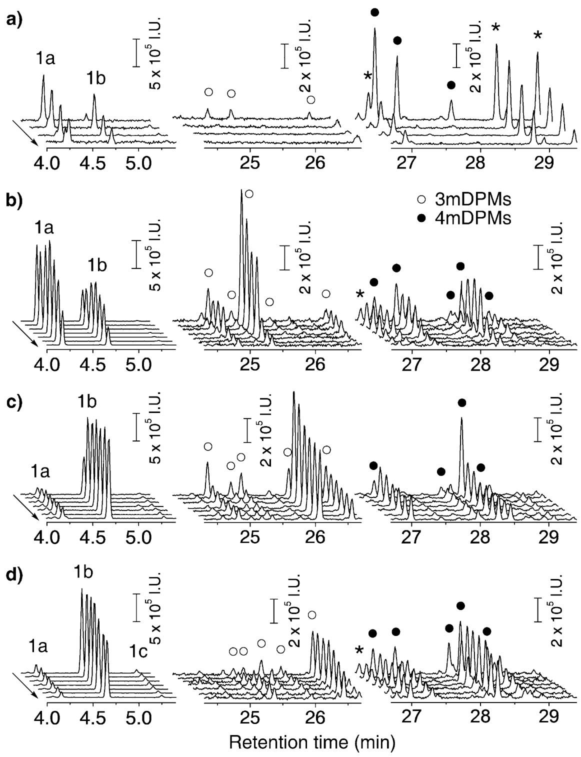

Figure 6. GC-MS chromatograms of the CH_2Cl_2 extracts from (a) H−Y, (b) H-ZSM-5, (c) H-ZSM-57, and (d) H-TNU-10 after *m*-xylene transformation at 473 K and 10.7 h^{-1} WHSV for 10 h on stream followed by flushing with N_2 (40 mL min^{-1}) at the same temperature for different times. The chromatograms from H−Y were obtained after flushing for 0, 2, 5, and 10 min, respectively, and those from the other three zeolites were measured after flushing for 0, 2, 5, 10, 30, 60, and 120 min, respectively. For simplicity, only the segments covering the TMB (peaks 1a−c), 3mDPM (○), and 4mDPM (●) species are shown. The peaks indicated by asterisks are assignable to methylphenanthrenes in comparison with the NIST database.[44]

Table 3. Product Distribution and Percentage of Bimolecular Pathway at 523 K and Low Conversions of an Equimolar Mixture of Hexadeuterated and Normal *p*-Xylenes over a Number of Zeolites with Different Framework Structures

			normalized TMB distribution (mol %)			
zeolite	*p*-xylene conversion (%)	mol % o-xylene$_{109}$[a]	1,2,3-TMB	1,2,4-TMB	1,3,5-TMB	% bimolecular isomerization[b]
H-TNU-9	6.0	3.5	0.0	100	0.0	10.5 (7.7)
H-MCM-22	3.2	4.0	0.0	100	0.0	12.0 (11.1)
H-NU-87	7.6	11.9	0.0	100	0.0	35.7 (30.8)
H-EU-1	8.8	1.7	0.0	100	0.0	5.1 (4.6)
H-IM-5	9.1	0.9	0.0	100	0.0	2.7 (2.3)
H-ZSM-5	7.0	0.3	0.0	100	0.0	0.9 (0.8)
H-ITQ-2	7.2	6.3	5.4	89.3	5.3	18.9 (17.5)
H-SUZ-4	3.9	0.5	0.0	0.0	0.0	1.5
H-TNU-10	5.6	0.2	0.0	100	0.0	0.6 (0.7)
H-ferrierite	2.1	1.0	0.0	100	0.0	3.0 (3.1)
H-ZSM-57	9.5	0.2	0.0	100	0.0	0.6 (0.5)
H-ZSM-22	2.0	0.5	0.0	100	0.0	1.5 (1.5)
H-ZSM-23	8.6	1.2	0.0	100	0.0	3.6 (3.4)
H−Y	8.2	27.4	2.8	91.4	5.8	82.2 (79.0)
H-beta	5.9	15.0	3.5	90.1	6.4	45.0 (43.3)
H-mordenite	4.6	5.6	7.2	85.9	6.9	16.8 (13.3)

[a] Mole percentage of o-xylene with a molecular mass of 109 produced. Calculated using the equation mol % o-xylene$_{109}$ = o-xylene$_{109}$/(o-xylene$_{106}$ + o-xylene$_{109}$ + o-xylene$_{112}$) × 10^2. [b] Percentage of bimolecular isomerization in the formation of o-xylene from p-xylene. Calculated using the equation % bimolecular isomerization = (mol % o-xylene$_{109}$)/(mol % o-xylene(100)$_{109}$) × 10^2, where mol % o-xylene(100)$_{109}$ is the mole percentage of o-xylene$_{109}$ yielding 100% bimolecular p-xylene isomerization. For details, see the text. The values in parentheses were calculated based on the normalized distribution of normal, tri-, hexa-, and nonadeuterated 1,2,4-TMB species with molecular masses of 120, 123, 126, and 129, respectively, produced over each zeolite (Supporting Information Table S2).

As found in the GC-MS data from H-TNU-9 and H-ZSM-5, the 3mDPM and 4mDPM signals from H-ZSM-57 and H-TNU-10 with an intersecting 10- and 8-ring pore system also show a decrease in intensity at the onset of flushing, coinciding with the initial increase of their 1,2,4-TMB signal. After some time, however, no further decrease in intensity of 3mDPM and 4mDPM signals is observed, which agrees well with no significant changes in the intensity of the 1,2,4-TMB signal during the rest of flushing time up to 120 min. This suggests that the 3mDPM and 4mDPM derivatives, as well as 1,2,4-TMB, formed in H-ZSM-57 and H-TNU-10 are more stable than those in H-TNU-9 and H-ZSM-5, probably due to the tighter build-up within the narrower pore system of the former two zeolites. In our view, their aromatic organic species may serve mainly as space-filling species, which may be a source of aromatic coke in the long run, rather than as reaction intermediates of *m*-xylene isomerization and disproportionation. If so, the high *p*-xylene selectivity observed for H-TNU-10 and H-ZSM-57 (Figure 2) cannot be a result of transition state shape selectivity but of product one. This is because they possess quite similar crystal morphologies and sizes to each other (Supporting Information Table S1). From the overall GC-MS results of our study, therefore, we can conclude that transition state and product shape selectivities are experimentally distinguishable from each other.

Table 3 lists the mole percentage (mol % o-xylene$_{109}$) of o-xylene with a molecular mass of 109 produced over all 16 known zeolite catalysts with different framework structures at conversion levels lower than 10% and the percentage of bimolecular pathway in xylene isomerization over each zeolite, which were determined from isotope labeling experiments using an equimolar mixture of normal and hexadeuterated p-xylenes with molecular mass of 106 (p-xylene$_{106}$) and 112 (p-xylene$_{112}$), respectively, at 523 K. This relatively low reaction temperature was selected because the 3mDPM and 4mDPM GC-MS signals, if observable from zeolites, show generally the strongest intensity at that temperature while being almost missing at 623 K. As can be seen in Supporting Information Scheme S2, the isotopically mixed xylene isomers with a molecular mass of 109 cannot be produced via a monomolecular 1,2-methyl shift. However, if the TMB isomers formed via p-xylene disproportionation transalkylate with another xylene molecule inside the zeolite pores, their formation could then be detected even at low conversions.

The catalytic data in Table 3 reveal that all medium-pore zeolites except H-ITQ-2 with a very high external surface area are characterized by 100% selectivity to 1,2,4-TMB, smaller than the other two TMB isomers, most likely due to product shape selectivity. H-mordenite exhibits the lowest 1,2,4-TMB selectivity among the zeolites employed in this study, but even its selectivity is greater than 80%. Therefore, we can assume that 1,2,4-TMB is the only TMB isomer generated by zeolite-catalyzed p-xylene disproportionation. Assuming neither further isomerization of initially formed 1,2,4-TMB molecules nor further disproportionation and transalkylation between them, in addition, the normal, tri-, hexa-, and nonadeuterated 1,2,4-TMB species with molecular masses of 120 (1,2,4-TMB$_{120}$), 123 (1,2,4-TMB$_{123}$), 126 (1,2,4-TMB$_{126}$), and 129 (1,2,4-TMB$_{129}$), respectively, produced through the statistical disproportionation between p-xylene$_{106}$ and p-xylene$_{112}$ with an equimolar ratio are distributed as 1:1:1:1. On the other hand, transalkylation between 1,2,4-TMB$_{120}$ and p-xylene$_{106}$ or p-xylene$_{112}$ cannot form o-xylene$_{109}$, which is also the case of 1,2,4-TMB$_{129}$. As can be seen in Supporting Information Scheme S3, o-xylene$_{109}$ is obtained when 1,2,4-TMB$_{123}$ and 1,2,4-TMB$_{126}$ transalkylate with either p-xylene$_{106}$ or p-xylene$_{112}$. However, not all isotopic 1,2,4-TMB$_{123}$ or 1,2,4-TMB$_{126}$ isomers can produce o-xylene$_{109}$: the two isomers isotopically mixed in positions 1 and 2 among the three possible 1,2,4-TMB$_{123}$ isomers generate this xylene isomer. Thus, taking into account the assumptions described above, the ideal mole percentage (mol % o-xylene$(100)_{109}$) of o-xylene$_{109}$ corresponding to 100% bimolecular isomerization in the formation of o-xylene from p-xylene over any zeolite catalyst can be calculated using the following simple equation:

$$\begin{aligned}&\text{mol\% } o\text{-xylene}(100)_{109}\\&\quad = \text{mol\%}(\text{1,2,4-TMB}_{123} + \text{1,2,4-TMB}_{126})\\&\qquad \times R(\text{1,2,4-TMB}(1,\,2)_{123/126})\end{aligned} \tag{1}$$

where mol % (1,2,4-TMB$_{123}$ + 1,2,4-TMB$_{126}$) is the mole percentage (50%) of 1,2,4-TMB$_{123}$ and 1,2,4-TMB$_{126}$ and R(1,2,4-TMB$(1,2)_{123/126}$) is the molar ratio (2/3) of the 1,2,4-TMB$_{123}$ or 1,2,4-TMB$_{126}$ isomers isotopically mixed in positions 1 and 2 to the three possible isomers. Then,

$$\text{mol\% } o\text{-xylene}(100)_{109} = 50\% \times 2/3 = 33.3\% \tag{2}$$

Therefore, the percentage of bimolecular isomerization in o-xylene formation over a particular zeolite, designated as percent bimolecular isomerization, is

$$\begin{aligned}&\%\text{ bimolecular isomerization}\\&\quad = (\text{mol\% } o\text{-xylene}_{109})/(\text{mol\% } o\text{-xylene}(100)_{109}) \times 10^2\%\\&\quad = (\text{mol\% } o\text{-xylene}_{109})/33.3\% \times 10^2\%\end{aligned} \tag{3}$$

As expected, H−Y containing supercages with a diameter of 12.0 Å shows the highest contribution (82%) of bimolecular pathway among the zeolites employed in this study. Also, H-beta with two intersecting 12-ring (5.6 Å × 5.6 Å and 6.6 Å × 6.7 Å) channels gives the second highest value (45%). As seen in Table 3, however, H-mordenite, an actually 1D 12-ring (6.5 Å × 7.0 Å) material, barely exhibits 17%, again confirming that the pore dimensionality of zeolites is another important factor governing the percentage of bimolecular pathway in xylene isomerization. Table 3 also shows that the contribution of bimolecular isomerization in o-xylene formation over medium-pore zeolites containing internal cavities larger than 10-rings is in the range of 5−36%, depending on their pore topology. Therefore, it is clear that bimolecular xylene isomerization is not always suppressed in medium-pore zeolites, which is in good agreement with the GC-MS results given above. The high percentage (36%) of H-NU-87 suggests that the external acid sites on this medium-pore zeolite play an important role in the bimolecular isomerization of p-xylene to o-xylene, which can be correlated with its relatively low p/o ratio (Table 2).

A similar interpretation can also be given to H-ITQ-2, because the amount (6.3%) of o-xylene$_{109}$ produced over this delaminated zeolite is fairly larger than that (4.0%) from its parent zeolite H-MCM-22. In contrast, ZSM-5 and IM-5 with mutually intersecting 10-ring channels only produce less than 1% of o-xylene$_{109}$, which is also the case of H-TNU-10 and H-ZSM-57 with two intersecting 10- and 8-ring channels. This indicates that the monomolecular 1,2-methyl shift mechanism is prevailing with all these four medium-pore zeolites, although the formation of 3mDPM and 4mDPM species in their confined pores is possible, as evidenced by GC-MS analyses. Finally, it is interesting to note that when the percentage of bimolecular isomerization in o-xylene formation over zeolites employed here is calculated based on the actual distribution (Supporting Information Table S2) of isotopic 1,2,4-TMB isomers with molecular masses ranging from 120 to 129 produced over each zeolite; no dramatic changes in its contribution were found, as seen in Table 3. This suggests that the extent of secondary isomerization and disproportionation of 1,2,4-TMB in p-xylene conversion is not so high.

4. CONCLUSIONS

The catalytic properties of 13 medium-pore zeolites with different framework topologies, together with three well-known large-pore zeolites, are compared in the isomerization and disproportionation of m-xylene, and all zeolite catalysts tested are subject to ex situ GC-MS analysis to identify the intermediates of these reactions. H-TNU-10 and H-ZSM-57 with intersecting 10- and 8-ring channels show considerably high p/o ratios compared with the ratio of H-ZSM-5. Also, no noticeable decrease in both m-xylene conversion and p/o ratio during the period of time on stream studied here is observed, suggesting their high potential as new isomerization catalysts. On the other hand, the GC-MS results presented here may be the first to experimentally verify that tri- and tetramethylated diphenylmethane species are real reaction intermediates of m-xylene isomerization and disproportionation. The formation of these dicyclic aromatic transition states is possible in medium-pore zeolites, if they contain large internal cavities or channel intersections, as well as in large-pore materials. Isotope labeling experiments during the p-xylene transformation allow us to reasonably determine the contribution of bimolecular pathway in xylene isomerization over each of zeolites employed here. The overall results of this study provide clear experimental evidence that product shape selectivity is responsible for the high p-xylene selectivity found in some medium-pore zeolites, whereas it is distinguishable from transition state shape selectivity.

■ ASSOCIATED CONTENT

Ⓢ Supporting Information

Additional information as noted in the text. This information is available free of charge via the Internet at http://pubs.acs.org.

■ AUTHOR INFORMATION

Corresponding Author

*E-mail: sbhong@postech.ac.kr.

Funding

This work was supported by the National Research Foundation of Korea (R0A-2007-000-20050-0 and 2011-0029806) and by the Ministry of Knowledge Economy of the Korean Government through the Inter-Metropolitan Cooperation Development Program (J000003936).

Notes

The authors declare no competing financial interest.

■ REFERENCES

(1) Chen, N. Y.; Degnan, T. F.; Smith, C. M. *Molecular Transport and Reaction in Zeolites: Design and Application of Shape Selective Catalysts*; VCH: 1994; p 173.
(2) Degnan, T. F. *J. Catal.* **2003**, *216*, 32.
(3) Vermeiren, W.; Gilson, J.-P. *Top. Catal.* **2009**, *52*, 1131.
(4) Camblor, M. A.; Hong, S. B. In *Porous Materials*; Bruce, D. W., O'Hare, D., Walton, R. I., Eds.; Wiley: Chichester, 2011; p 265.
(5) Csicsery, S. M. *J. Org. Chem.* **1969**, *34*, 3338.
(6) Gnep, N. S.; Tejada, J.; Guisnet, M. *Bull. Soc. Chim. Fr. I* **1982**, 5.
(7) Corma, A.; Sastre, E. *J. Catal.* **1991**, *129*, 177.
(8) Weitkamp, J.; Ernst, S. *Catal. Today* **1994**, *19*, 107.
(9) Gnep, N. S.; Morin, S.; Guisnet, M. *J. Catal.* **1996**, *159*, 296.

(10) Guisnet, M.; Gnep, N. S.; Morin, S. *Microporous Mesoporous Mater.* **2000**, *35–36*, 47.
(11) Clark, L. A.; Sierka, M.; Sauer, J. *J. Am. Chem. Soc.* **2003**, *125*, 2136.
(12) Demuth, T.; Raybaud, P.; Lacombe, S.; Toulhoat, H. *J. Catal.* **2004**, *222*, 323.
(13) Martens, J. A.; Pérez-Pariente, J.; Sastre, E.; Corma, A.; Jacobs, P. A. *Appl. Catal.* **1988**, *45*, 85.
(14) Corma, A.; Corell, C.; Llopis, F. J.; Martínez, A.; Pérez-Pariente, J. *Appl. Catal., A* **1994**, *115*, 121.
(15) Adair, B.; Chen, C.-Y.; Wan, K.-T.; Davis, M. E. *Microporous Mater.* **1996**, *7*, 261.
(16) Jones, C. W.; Zones, S. I.; Davis, M. E. *Appl. Catal., A* **1999**, *181*, 289.
(17) Corma, A.; Chica, A.; Guil, J. M.; Llopis, F. J.; Mabilon, G.; Perdigón-Melón, J. A.; Valencia, S. *J. Catal.* **2000**, *189*, 382.
(18) Moliner, M.; González, J.; Portilla, M. T.; Willhammar, T.; Rey, F.; Llopis, F. J.; Zou, X.; Corma, A. *J. Am. Chem. Soc.* **2011**, *133*, 9497.
(19) Clark, L. A.; Sierka, M.; Sauer, J. *J. Am. Chem. Soc.* **2004**, *126*, 936.
(20) Baerlocher, Ch.; McCusker, L. B. *Database of Zeolite Structures*, http://www.iza-structure.org/databases/.
(21) De Vos, D. E.; Ernst, S.; Perego, C.; O'connor, C. T.; Stöcker, M. *Microporous Mesoporous Mater.* **2002**, *56*, 185.
(22) International Zeolite Association, Catalysis Commission. http://www.iza-online.org/catalysis/.
(23) Weiss, U.; Weihe, M.; Hunger, M.; Karge, H. G.; Weitkamp, J. *Stud. Surf. Sci. Catal.* **1997**, *105*, 973.
(24) Arsenova-Härtel, N.; Bludau, H.; Haag, W. O.; Karge, H. G. *Microporous Mesoporous Mater.* **2000**, *35–36*, 113.
(25) Arsenova-Härtel, N.; Bludau, H.; Schumacher, R.; Haag, W. O.; Karge, H. G.; Brunner, E; Wild, U. *J. Catal.* **2000**, *191*, 326.
(26) Huang, J.; Jiang, Y.; Marthala, V. R. R.; Bressel, A.; Frey, J.; Hunger, M. *J. Catal.* **2009**, *263*, 277.
(27) Min, H.-K.; Chidambaram, V.; Hong, S. B. *J. Phys. Chem. C* **2010**, *114*, 1190.
(28) Min, H.-K.; Hong, S. B. *J. Phys. Chem. C* **2011**, *115*, 16124.
(29) Hong, S. B.; Min, H.-K.; Shin, C.-H.; Cox, P. A.; Warrender, S. J.; Wright, P. A. *J. Am. Chem. Soc.* **2007**, *129*, 10870.
(30) Corma, A.; Corell, C.; Pérez-Pariente, J. *Zeolites* **1995**, *15*, 2.
(31) Shannon, M. D.; Casci, J. L.; Cox., P. A.; Andrews., S. J. *Nature* **1991**, *353*, 417.
(32) Souverijns, W.; Rombouts, L.; Martens, J. A.; Jacobs, P. A. *Microporous Mater.* **1995**, *4*, 123.
(33) Lee, S.-H.; Lee, D.-K.; Shin, C.-H.; Park, Y.-K.; Wright, P. A.; Lee, W. M.; Hong, S. B. *J. Catal.* **2003**, *215*, 151.
(34) Paik, W. C.; Shin, C.-H.; Hong, S. B. *Chem. Commun.* **2000**, 1609.
(35) Hong, S. B.; Lear, E. G.; Wright, P. A.; Zhou, W.; Cox, P. A.; Shin, C.-H.; Park, J.-H.; Nam, I.-S. *J. Am. Chem. Soc.* **2004**, *126*, 5817.
(36) Lee, S.-H.; Lee, D.-K.; Shin, C.-H.; Paik, W. C.; Lee, W. M.; Hong, S. B. *J. Catal.* **2000**, *196*, 158.
(37) Ernst, S.; Weitkamp, J.; Martens, J. A.; Jacobs, P. A. *Appl. Catal.* **1989**, *48*, 137.
(38) Wang, B.; Gao, Q.; Gao, J.; Ji, D.; Wang, X.; Suo, J. *Appl. Catal., A* **2004**, *274*, 167.
(39) Corma, A.; Fornés, V.; Martínez-Triguero, J.; Pergher, S. B. *J. Catal.* **1999**, *186*, 57.
(40) Emeis, C. A. *J. Catal.* **1993**, *141*, 347.
(41) Guisnet, M.; Magnoux, P. *Appl. Catal.* **1989**, *54*, 1.
(42) Min, H.-K.; Park, M. B.; Hong, S. B. *J. Catal.* **2010**, *271*, 186.
(43) Lee, J.-H.; Park, M. B.; Lee, J. K.; Min, H.-K.; Song, M. K.; Hong, S. B. *J. Am. Chem. Soc.* **2010**, *132*, 12971.
(44) NIST Chemistry Web book, http://webbook.nist.gov/chemistry/.
(45) Baertsch, C. D.; Funke, H. H.; Falconer, J. L.; Noble, R. D. *J. Phys. Chem. B* **1996**, *100*, 7676.
(46) Mihindou-Koumba, P. C.; Comparot, J.-D.; Laforge, S.; Magnoux, P. *J. Catal.* **2008**, *255*, 324.
(47) *CRC Standard Mathematical Tables and Formulae*, 31th ed.; Zwillinger, D., Ed.; CRC: Boca Raton, 2003.
(48) Hammonds, K. D.; Heine, V.; Dove, M. T. *J. Phys. Chem. B* **1998**, *102*, 1759.
(49) Sartbaeva, A.; Wells, S. A.; Treacy, M. M. J.; Thorpe, M. F. *Nat. Mater.* **2006**, *5*, 962.
(50) Hong, S. B.; Lee, S.-H.; Shin, C.-H.; Woo, A. J.; Alvarez, L. J.; Zicovich-Wilson, C. M.; Camblor, M. A. *J. Am. Chem. Soc.* **2004**, *126*, 13742.
(51) Shin, J.; Bhange, D. S.; Camblor, M. A.; Lee, Y.; Kim, W. J.; Nam., I.-S.; Hong, S. B. *J. Am. Chem. Soc.* **2011**, *133*, 10587.
(52) Llopis, F. J.; Sastre, G.; Corma, A. *J. Catal.* **2004**, *227*, 227.
(53) Park, S.-H.; Rhee, H.-K. *Catal. Today* **2000**, *63*, 267.
(54) Streitwieser, A.; Reif, L. *J. Am. Chem. Soc.* **1960**, *82*, 5003.
(55) Lanewala, M. A.; Bolton, A. P. *J. Org. Chem.* **1969**, *34*, 3107.
(56) Jacobs, P. A.; Martens, J. A. *Stud. Surf. Sci. Catal.* **1991**, *58*, 445.
(57) Santilli, D. S. *J. Catal.* **1986**, *99*, 327.
(58) Svelle, S.; Olsbye, U.; Lillerud, K.-P.; Kolboe, S.; Bjørgen, M. *J. Am. Chem. Soc.* **2006**, *126*, 5618.
(59) Sievers, C.; Onda, A.; Guzman, A.; Otillinger, K. S.; Olindo, R.; Lercher, J. A. *J. Phys. Chem. C* **2007**, *111*, 210.
(60) Cerqueira, H. S.; Magnoux, P.; Martin, D.; Guisnet, M. *Appl. Catal., A* **2001**, *208*, 359.
(61) Guisnet, M.; Magnoux, P. *Appl. Catal., A* **2001**, *212*, 83.